A&A 676, A58 (2023)
https://doi.org/10.1051/0004-6361/202345909

Astronomy & Astrophysics
Special issue

Solar Orbiter First Results (Nominal Mission Phase)

Anisotropies of solar energetic electrons in the MeV range measured with Solar Orbiter/EPD/HET

S. Fleth[1], P. Kuehl[1], A. Kollhoff[1], R. F. Wimmer-Schweingruber[1], B. Heber[1], J. Rodríguez-Pacheco[2], and N. Dresing[3]

[1] Institute of Experimental & Applied Physics, Kiel University, 24118 Kiel, Germany
e-mail: fleth@physik.uni-kiel.de
[2] Space Research Group/Universidad de Alcalá, Madrid, Spain
[3] Department of Physics and Astronomy, University of Turku, Turku, Finland

Received 13 January 2023 / Accepted 2 April 2023

ABSTRACT

Aims. This study analyses relativistic electron measurements obtained by the High Energy Telescope (HET) aboard Solar Orbiter in the energy range from 200 keV to above 10 MeV. Caveats of these measurements are discussed. The purpose of this study is to analyse anisotropies of relativistic solar energetic electrons utilising the different viewing directions of HET.
Methods. We identified time periods of interest, that is, those with enhanced electron flux due to a significant solar component, and composed a list of these time periods, including additional observations such as maximum energy and flux as well as the first-order anistropy.
Results. This study provides an overview of HET measurements of MeV electrons and a list of time periods of enhanced flux of relativistic solar electrons, 21 in total. For the first time with Solar Orbiter/EPD/HET, the anisotropies of high-energy electrons have been measured. Specifically, we find three time periods with significant anisotropy above 1 MeV within 0.5 au.

Key words. Sun: corona – Sun: heliosphere – Sun: particle emission – instrumentation: detectors – methods: data analysis

1. Introduction

Most electrons in solar energetic particle (SEP) events are believed to be accelerated by flares. These flares impulsively release energy that was stored in non-potential coronal magnetic fields, presumably by magnetic reconnection. This release emits electromagnetic radiation over the whole wavelength range from radio to gamma rays (Fletcher et al. 2011). According to Reames (1999) among impulsive events associated with the flare there are also events associated with shocks driven by coronal mass ejections (CMEs). These events inject SEPs over a longer time span and therefore have a larger angular extent then the impulsive events. However, it is unclear as to whether or not shocks can accelerate electrons to energies exceeding hundreds of keV or even MeV. It is not unusual for flares to appear during a CME-associated event and this makes it difficult to separate the different components of the flare-related and shock-related particle acceleration and to identify which of them might be dominating the particle-energising process in some events (e.g., Kouloumvakos et al. 2015). Kahler et al. (2007) suggested that long-lasting electron anisotropies could be an indication for electron-shock acceleration because of the temporally extended electron injections close to the Sun that can be associated with these anisotropies. However, these temporally extended electron injections could also be produced by other processes, such as ongoing acceleration or trapping in post-flare loops (e.g., Klein et al. 2005) or CME–CME interaction regions (e.g., Gopalswamy et al. 2004; Dresing et al. 2018). These traps could be the reason for an ongoing electron injection because of a continuous leakage of electrons. The work of Dresing et al. (2022) shows that the shock of CMEs is as significant for relativistic electrons as it is for the high-energy protons. This might lead to a common shock-related acceleration process for relativistic electrons. The near-relativistic electrons do not show the same dependencies as the relativistic electrons and therefore seem to be less effected by the shock and more effected by a flare-related process. Also the numerical simulations of Guo & Giacalone (2015) show that diffusive shock acceleration can accelerate electrons to relativistic energies. The conditions for this are quasi-parallel shocks when large-amplitude magnetic fluctuations exist. In addition, the work of Amano et al. (2020) revealed evidence for stochastic shock drift acceleration of electrons. This might be due to intense whistler waves in the transition layer. This model is supported by two independent measurements. However, this question is still the topic of a long-lasting debate and a definitive answer remains to be found.

Solar Orbiter is an ESA-led mission of international collaboration with NASA (Müller et al. 2013, 2020) designed to investigate how the Sun creates and controls the heliosphere, and why solar activity changes with time. One of its top-level science questions is how solar eruptions produce energetic particle radiation that fills the heliosphere (Müller et al. 2020). The Energetic Particle Detector (EPD; Rodríguez-Pacheco et al. 2020) with its four different sensors – briefly summarised in Sect. 2 – provides measurements to tackle this question. Section 2 also describes the High-Energy Telescope (HET) used for this work as well as a patch for HET that was uploaded in October 2021. We provide an overview of observations of flux enhancements of high-energy electrons. The method used to identify these enhancements is described in Sect. 3, a list of the identified time periods is provided, and an example is discussed in detail in Sect. 4.

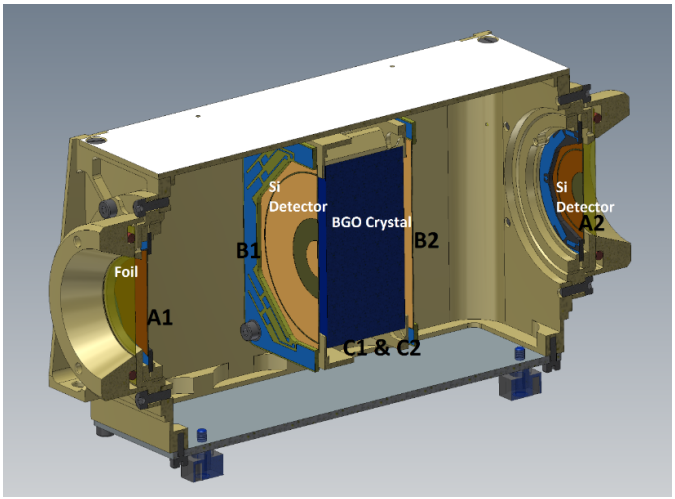

Fig. 1. Cross-section of an HET unit (Rodríguez-Pacheco et al. 2020).

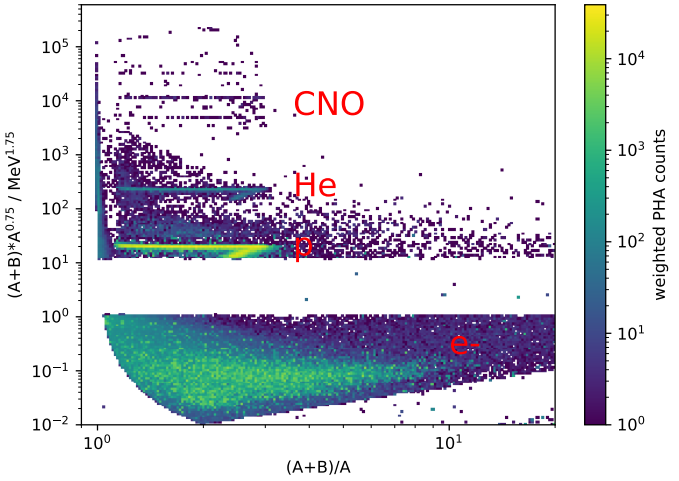

Fig. 2. Modified PIN_{AB} defined in Eq. (1) as a function of measured energy divided by the energy loss in the first detector. The gap in PIN_{AB} between 1 and 19 separates electrons from ions, and data for this range are not transmitted. At larger PINs, the tracks of hydrogen, helium, CNO, and other heavy elements can be identified.

2. Instrumentation

The EPD suite on Solar Orbiter consists of four different instruments, the SupraThermal Electrons and Protons sensor (STEP), the Electron Proton Telescope (EPT), the Suprathermal Ion Spectrograph (SIS), and the HET, which together cover energy ranges from several keV up to GeV for ions and from a few keV to MeV for electrons. EPT and HET are combined in one common electronics box and two near-identical units are located on the spacecraft with orthogonal viewing directions (see Fig. 1 in Rodríguez-Pacheco et al. 2020). Additional information and updates are also given in Wimmer-Schweingruber et al. (2021).

The HET instrument is designed to cover the energy range from a few MeV/nuc up to a few hundred MeV/nuc for ions (see Fig. 3 in Rodríguez-Pacheco et al. 2020) and relativistic electrons to above 10 MeV.

Each HET unit is a double-sided telescope stack consisting of a central bismuth germanium oxide (BGO) scintilator (C) and two solid state detectors (SSDs) on each side (A_i and B_i), as shown in Fig. 1. The four SSDs are segmented, with the outer segments acting as anticoincidence. HET utilises the $\mathrm{d}E/\mathrm{d}x - E$ method and the $\mathrm{d}E/\mathrm{d}x$–$\mathrm{d}E/\mathrm{d}x$ method for stopping and penetrating particles, respectively. For stopping particles, the following coincidences are utilised (for details, see Rodríguez-Pacheco et al. 2020), where indices 1 or 2 can be exchanged for the two viewing directions (forward/backward) of HET:

- $A_1\ B_1\ \overline{C}\ \overline{B_2 A_2}$: Particles that stop in detector B or in detector C with an energy loss below the threshold value in the BGO scintillator.
- $A_1\ B_1\ C\ \overline{B_2 A_2}$: Particles that stop in the BGO C and for which the energy loss SSD B_2 is smaller than the threshold value.

Thus, for the above coincidences, the total kinetic energy loss in the instrument of a particle and its direction (forward/backward) are known and therefore the two HET units provide a total of four viewing directions (sun, anti-sun, north, south), which allows us to also investigate anisotropies of high-energy electrons. The quantity $\mathrm{d}E/\mathrm{d}x \cdot E = m \cdot z^2$ is normally well defined for stopping ions and has been termed the particle identification number (PIN; see e.g., Terasa et al. 2013; Kühl & Heber 2019, and references therein) but this quantity is not well defined for electrons. We therefore define modified pins,

$$\mathrm{PIN}_{AB} = (\mathrm{d}E/\mathrm{d}x_{A_i})^{0.75} \cdot E_{A_1+B_1}, \tag{1}$$

and

$$\mathrm{PIN}_{ABC} = (\mathrm{d}E/\mathrm{d}x_{\min(A_i,\,B_1)})^{1.5} \cdot E_{A_1+B_1+C}, \tag{2}$$

which are used throughout this study. The modified PIN_{AB} for the first coincidence is displayed in Fig. 2 as a function of the total measured energy divided by the energy loss in the first SSD.

Here, it is evident that the ion tracks of hydrogen, helium, carbon, nitrogen, and oxygen are well separated from each other and that particles stopping in B_1 can be identified as electrons if

$$10^{-3}\,\mathrm{MeV}^{1.75} < \mathrm{PIN}_{AB} < 1\,\mathrm{MeV}^{1.75}. \tag{3}$$

Data from particles with PIN_{AB} above the upper threshold for electrons and below the lower threshold for protons are not sent to Earth in the EPD telemetry stream because they contain no physical information. We note that the hydrogen and helium tracks indicate that the threshold in the BGO scintillator is rather high, because the track of SSD B_1 penetrating protons and helium is well developed (see e.g., Kühl et al. 2020, and references therein). Similarly, we can identify particles stopping in C as electrons if the condition

$$2 \times 10^{-3}\,\mathrm{MeV}^{2.5} < \mathrm{PIN}_{ABC} < 2\,\mathrm{MeV}^{2.5} \tag{4}$$

is fulfilled (see Fig. 3). Comparing Fig. 2 with Fig. 3 reveals two additional features in the ABC coincidence that are not seen in the AB coincidence: one feature at high values of the seen energy loss divided by the minimum of the energy losses in A and B, and another at low values. As both figures represent the same particle-identification method, namely the $\mathrm{d}E/\mathrm{d}x - E$ method, these differences are not expected.

In order to investigate this feature in more detail, we show the sum of the energy losses in detectors A_1 and B_1 as a function of the deposited energy in the BGO (C) in Fig. 4, for all data recorded until October 2021. The red dashed lines present isolines of constant total measured energies with the energy edges of the ABC coincidence given in Table 1. We note that

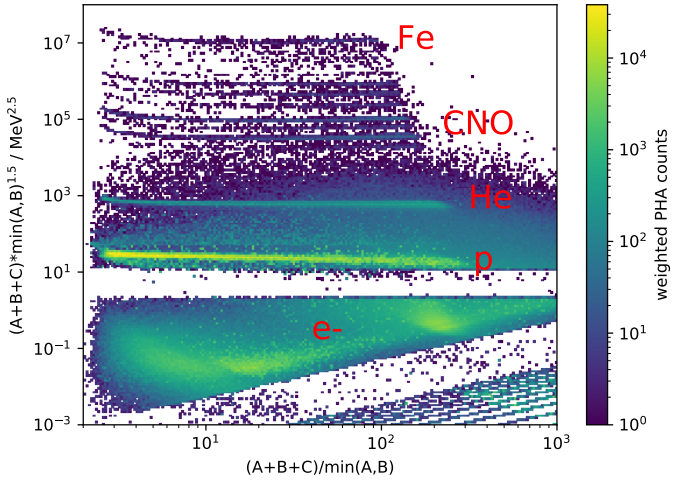

Fig. 3. Modified PIN defined in Eq. (2) as a function of the measured energy divided by the energy loss in the first detector. This figure includes particles stopping in the central BGO detector (C), while Fig. 2 shows particles stopping in detector B. The gap with PIN_{ABC} between 0.5 and 2 separates the electrons from ions, and data for this range are not transmitted. At larger PINs, the tracks of hydrogen, helium, CNO, and other heavy elements can be identified.

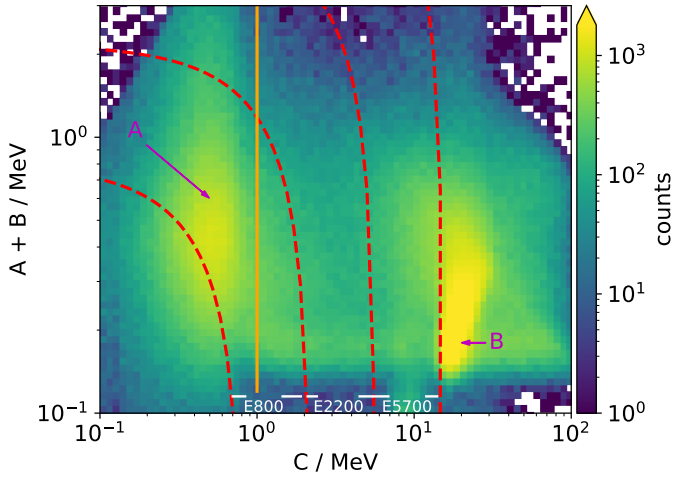

Fig. 4. PHA data of electrons stopping in C measured until October 2021. The red curves represent the energy ranges of the three electron channels (see Table 1) while the orange line indicates the absolute energy threshold in C introduced with a patch in October 2021. The populations A and B are discussed in the text.

two distinct populations that are not related to electrons can be clearly identified: Population A, which dominates the counts observed in the lowest channel (E800) with energy losses in C $E_C < 1\,\mathrm{MeV}$; and population B, with slightly higher energy losses in C $E_C > 15\,\mathrm{MeV}$ than what is allowed for the highest electron channel with $5\,\mathrm{MeV} \leq E \leq 15\,\mathrm{MeV}$.

The first has been found to be caused by electronic noise of the signal in C, which has not been correctly characterised and considered in the trigger logic of the instrument. Electrons stopping in B were therefore falsely identified as stopping in C simply due to noise and the counts of the flux of the E200 electron channel were underestimated, while the flux in the E800 channel was overestimated. The latter is caused by penetrating protons that are not correctly identified as penetrating and it can be seen that they barely contribute to the highest electron channel. Therefore, a patch was uploaded on October 12, 2021, introducing an absolute threshold in C of $E_C = 1\,\mathrm{MeV}$ for any ABC coincidence. This means that every particle to the left of the orange line shown in Fig. 4 would now be counted in the AB coincidence.

All particles identified as electrons in either of those coincidences are processed on board in two 1D histograms of their total deposited energy ($A+B$ and $A+B+C$). Based on these two histograms, the electron flux within the energy ranges given in Table 1 is derived. We note that these energies are different from the primary energies.

The impact of the patch can be clearly seen in Fig. 5, which shows the fluxes of the different sunward HET electron channels in addition to Solar Orbiters radial distance to the Sun. Clearly, the fluxes of the E200 and E800 channels differ before and after the patch (indicated by the black line). Furthermore, various short-term increases caused by SEP events can be identified across the different channels.

Table 1. HET electron channels and their corresponding coincidences (stopping in B or C).

Channel	Coincidence	E_{min}	E_{max}
E200	AB	0.2 MeV	1.0 MeV
E800	ABC	0.8 MeV	2.2 MeV
E2200	ABC	2.2 MeV	5.7 MeV
E5700	ABC	5.7 MeV	15.3 MeV

Notes. E_{min} and E_{max} give the lower and upper threshold for the total measured energy loss for each channel (for more detail see text).

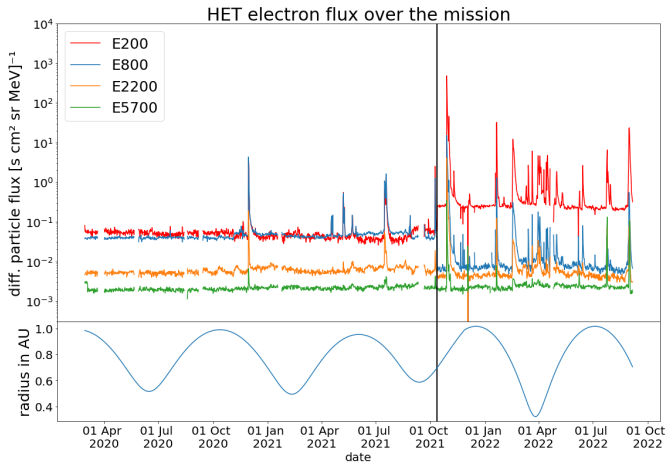

Fig. 5. Overview of the nominal electron flux measured with HET sun over the whole mission in 12 h time resolution. The lower panel shows the radial distance of Solar Orbiter to the Sun. The date of the patch is indicated as a black line.

3. Identification of time periods with enhanced flux

We investigated HET measurements obtained since the launch of Solar Orbiter in February 2020 until September 2022 in order to identify periods of enhanced flux of relativistic solar energetic electrons. The time period before the patch requires complex further investigation in order to identify time periods of enhanced flux for the reasons explained in Sect. 2. Figure 6 shows the nominal electron flux over the time period from 12 October until 5 September in 3 hour time resolution. The start times of each

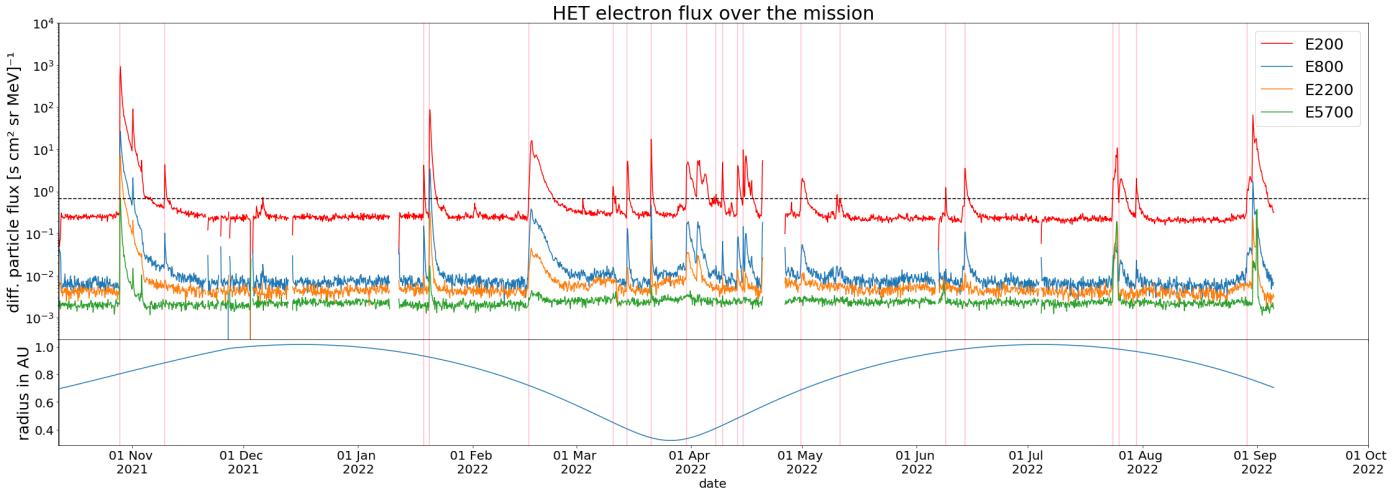

Fig. 6. Overview of the nominal electron flux over the time period from 12 October until 5 September in 3 h time resolution. The start time of each time period of enhanced flux that we find is highlighted with a pink vertical line. The lower panel shows the radial distance of Solar Orbiter to the Sun.

of the time periods of enhanced flux that we find are highlighted with pink vertical lines.

As the lowest energy channel of HET, the AB channel (E200) in the sun direction is most sensitive to relativistic solar electrons due to the usual soft-energy spectrum (Mewaldt et al. 2005), the identification scheme is based on these measurements (red curve in Fig. 6). If the flux rises in this channel, a time period of enhanced relativistic solar energetic electron flux is identified. In a second step, we identified the highest energy electron channel.

A threshold was needed to simply distinguish between time periods with enhanced flux and background. For this purpose, the measured flux of the E200 electron channel over the time period from 12 October until 5 September of the mission is shown in a histogram in Fig. 7. For the sake of simplicity, the distribution has been fitted using a Gaussian function,

$$a * \exp(-(x - x_0)^2/(2 * \sigma^2)), \tag{5}$$

in order to represent the fluxes in the absence of SEPs, where a is the maximum on the y-axis, x_0 is the mean value, and σ is the standard deviation. We expect the background to be constant in this simple approach, and with this assumption the background would have the form of a Poisson distribution. This distribution turns into a Gaussian function for sufficiently large N. The threshold for SEP identification after the patch was then defined as

$$x_0 + 4 * \sigma = 0.668\,(\mathrm{s\,cm^2\,sr\,MeV})^{-1}. \tag{6}$$

Because of the high activity of the Sun during the month of April, we tested the use of different multiplicands for the sigma. This shows the simple approach that was made with this kind of method and we note that the identified times should not be interpreted as onset times of events.

We identified time periods where these thresholds are exceeded for more than 100 min (10 data points with a time resolution of 10 min). Therefore, time periods where these thresholds are exceeded but that do not last 100 min will be missed with this method. The end of a period is determined when the flux in that time period of enhanced flux drops below $x_0 + \sigma$ and for at least 20 min. Because of this procedure, the determined start and end times of the time periods should not be understood as start and end times of a specific SEP event, but rather active time periods

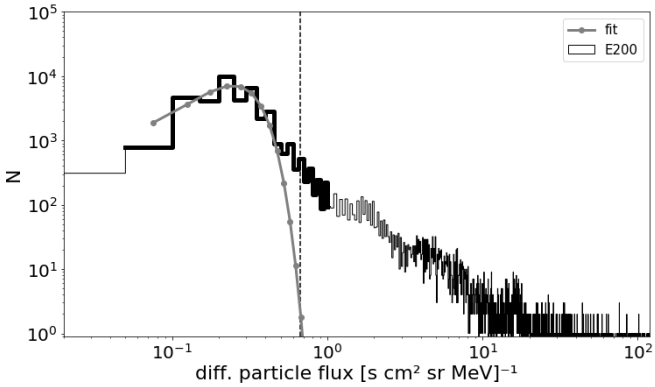

Fig. 7. Histogram of flux based on 10 min time resolution of the E200 channel over the entire mission. A highlighted area (thicker curve) of the histogram shows the predicted background energy range. The Gaussian fit can be seen as a curve in the energy range of the highlighted area. The thresholds found are shown as vertical lines.

that could include multiple SEP events. This also means that if particles of a second injection arrive at the spacecraft before the flux of a previous event decreases below $x_0 + \sigma$, the method will further extend the time interval, and the second SEP event will not have an individual entry in the list but will be included in the entry of the previous event. For this reason, we talk about time periods of enhanced flux rather then events. In order to separate those individual events, a more detailed study of each time period is necessary.

A list of the identified time periods is given in Table 2. This list provides a start time, an end time, the E200 peak flux in this period, the energy of the highest HET electron channel that has seen fluxes above the threshold of this channel, the longitude, the latitude, the distance from Solar Orbiter to the Sun, and the first-order anisotropy A_1. The latter is derived with the weights of the flux $I(\mu)$ for all four viewing directions measured at different pitch angles μ, as done by Brüdern et al. (2018):

$$A_1 = 3 * \frac{\sum_{n=1}^{4}(I(\mu) * \cos(\mu))}{\sum_{n=1}^{4} I(\mu)}, \tag{7}$$

where the factor of 3 can be explained by describing a gyrotropic pitch-angle distribution (PAD; e.g., Agueda & Lario 2016). Due

Table 2. Time periods with enhanced electron flux in the E200 channel.

Start	End	F_{peak} $(s\,cm^2\,sr\,MeV)^{-1}$	E_{max}	Long. °	Lat. °	r AU	A_1
2021-10-28 15:40	2021-11-07 02:40	1430	E5700	33	−3	0.8	<1
2021-11-09 17:20	2021-11-11 02:20	9	E800	47	−2	0.88	<1
2022-01-18 17:50	2022-01-19 07:30	8	E800	102	2	0.93	<1
2022-01-20 06:20	2022-01-22 22:40	176	E5700	103	2	0.92	<1
2022-02-16 03:50	2022-02-24 04:10	36	E800	130	3	0.72	–
2022-03-10 21:10	2022-03-11 18:00	3	E200	177	3	0.45	<1
2022-03-14 17:40	2022-03-15 20:00	9	E800	−168	2	0.41	<1
2022-03-21 05:30	2022-03-22 05:30	42	E2200	−135	1	0.34	>1
2022-03-30 17:40	2022-04-06 10:50	10	E800	−75	−2	0.34	<1
2022-04-07 18:00	2022-04-08 09:40	1	E800	−34	−3	0.41	<1
2022-04-09 11:40	2022-04-10 05:00	95	E800	−27	−3	0.43	>1
2022-04-13 13:10	2022-04-14 22:40	6	E800	−13	−3	0.48	<1
2022-04-15 03:00	2022-04-18 12:00	51	E2200	−9	−3	0.50	>1
2022-04-30 18:20	2022-05-02 15:10	4	E200	22	−2	0.69	<1
2022-05-11 04:50	2022-05-11 08:20	1	E200	35	−2	0.79	<1
2022-06-08 20:10	2022-06-09 03:10	3	E200	60	−0.23	0.97	<1
2022-06-14 01:00	2022-06-15 14:30	9	E800	64	−0.04	0.98	<1
2022-07-23 23:40	2022-07-25 13:50	116	E200	91	1	0.99	–
2022-07-25 18:40	2022-07-28 02:30	5	E200	93	1	0.98	–
2022-07-30 08:20	2022-07-31 01:00	3	E200	96	2	0.96	–
2022-08-29 08:20	2022-09-04 10:30	126	E800	123	3	0.77	–

Notes. The first and second columns give the start and end time of the period, respectively. In the third column, the peak flux of the time period is provided in units of $(s\,cm^2\,sr\,MeV)^{-1}$. In addition, the highest energy channel that has observed fluxes above its individual threshold is shown in column four and Solar Orbiter's longitude, latitude, and radial distance to the Sun are given in columns five, six, and seven, respectively. The eighth column shows if the anisotropie A_1 in a time window of 30 min before the start until 30 min after the start of the time period with enhanced flux in 1 min time resolution had at least five values above 1 or less than −1 (>1). If this is not the case, this is indicated with <1, or a dash if insufficient or no data were available (for more detail see Sect. 4).

to limited counting statistics in the higher energy channels, the anisotropies given in the table have been derived for the E200 channel. However, we would not expect large energy dependences in the anisotropies in between the HET electron channels, because all of them are measuring near-relativistic electrons, which show no energy dependences in the mean free path (Dröge 2000).

The value >1 indicates that the anisotropy in a window of 30 min before the start until 30 min after the start of the time period of enhanced flux in 1 min time resolution has at least five values above 1 or below −1. Otherwise, anistropy is given a value of <1. A dash (−) signifies that A_1 could not be calculated because of insufficient or missing data. This list shows that we find 21 active times where the flux of the E200 channel of HET rises above the threshold. In addition, we find three time periods that show clear anisotropies.

4. Example: April 15, 2022

For every time period that we find with enhanced flux, we provide a plot that gives a clear overview, which should allow the reader to quickly understand what is happening during these times. We present measurements taken on April 15, 2022, as an example of a period with enhanced flux. The top two panels of Fig. 8 show fluxes of electrons (top) and protons (second from top) measured by the sunward-pointing telescope. All four electron energy channels of HET and the highest energy channel of EPT are shown (Rodríguez-Pacheco et al. 2020). We note that protons contribute to the measurements of EPT during the shaded time periods. The second panel only shows a selection of HET energy channels as well as the EPT 465 keV channel. The particles measured by this telescope are streaming away from the Sun, approximately along the nominal Parker spiral. The third (fourth) panel from the top shows solar wind speed (kinetic temperature and density) measured by the Solar Wind Analyser (SWA; Owen et al. 2020), and the fifth panel shows magnitude, elevation, and azimuth angle of the interplanetary magnetic field (IMF) measured by the Solar Orbiter magnetometer (MAG; Horbury et al. 2020). Data from HET and MAG were combined to calculate the pitch angles with a time resolution of 1 min for all four viewing directions of HET, as shown in the bottom panel. The pitch angles are colour coded according to the flux measured in the E200 channel.

Measurements of the anisotropy during a period with enhanced flux are of special interest as they help to disentangle signatures of particle acceleration and transport. However, not many instruments are capable of providing anisotropies for electrons in the MeV range. To our knowledge the only observed anisotropies in this energy range were made with the E6 experiment on the Helios mission (Wibberenz et al. 1989; Hucke 1990) and with Parker Solar Probe (Mitchell et al. 2021). With the four viewing directions of HET, EPD now allows such measurements to also be performed with Solar Orbiter. The top (second) panel of Fig. 9 shows the flux measured by the E200 (E800) electron channels in all four directions in 1 min time resolution around the beginning of the time period of 15 April, 2022. The bottom panel shows the anisotropy derived for these channels using MAG data in 1 min time resolution. The anisotropy was calculated only if all viewing directions had at least two counts, and therefore it was not possible to cover the whole period. Nevertheless, the

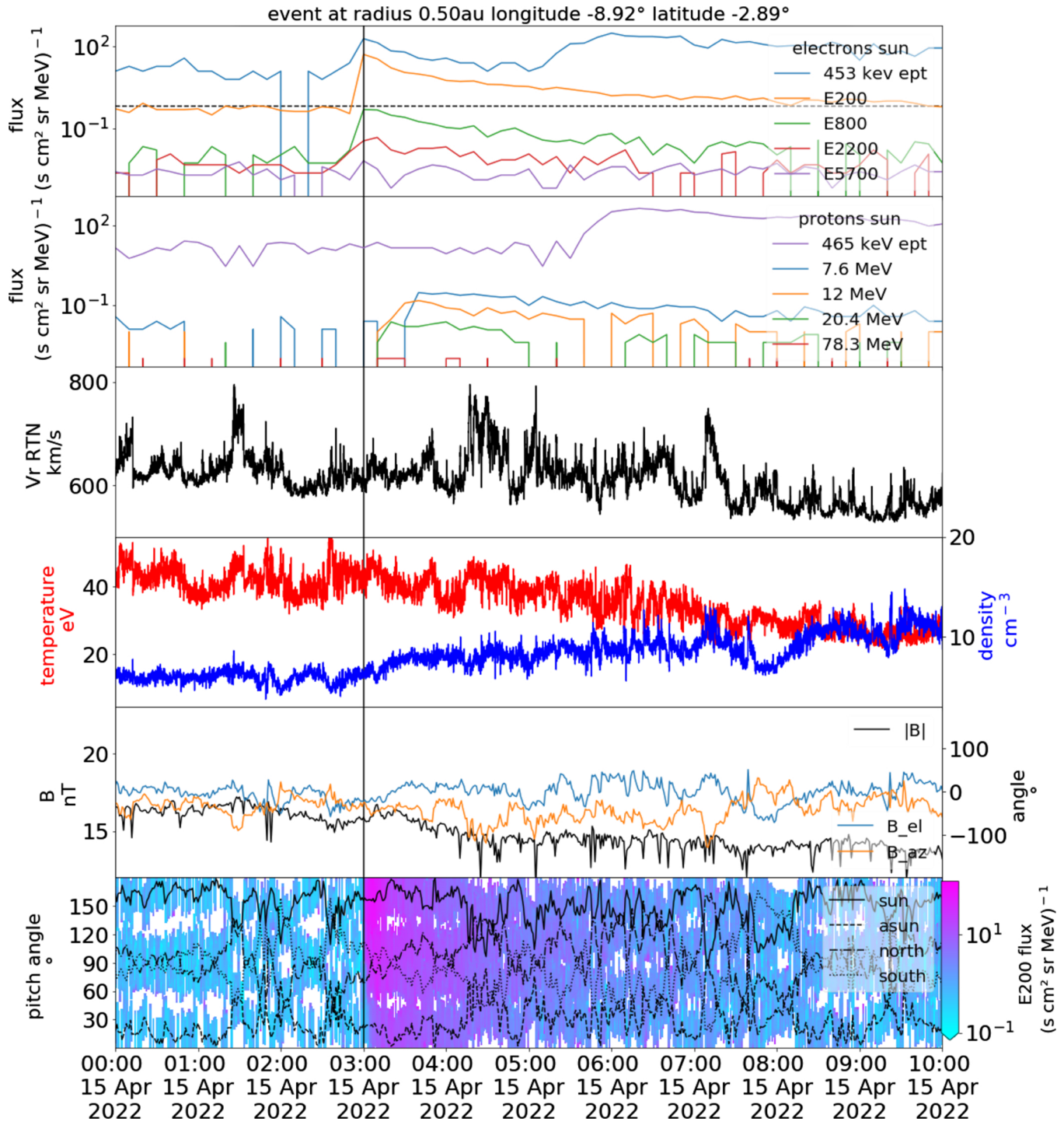

Fig. 8. Overview plot showing an example event from our list. The top panel shows the flux of all electron channels of HET and one electron channel of EPT for comparison. The black horizontal line shows the threshold of the E200 channel. The second subplot shows some of the proton channels of HET and one of EPT. Contamination might be seen here. Data from SWA are used in the third and fourth panels for the solar wind speed and the temperature and density. The MAG data are used for the fifth and sixth panels to show the different magnetic field values and the pitch angle of all viewing directions, respectively. In addition, the flux of the E200 channel is plotted alongside the pitch angels and is colour coded. The vertical black line shows the start time we find. The MAG data have a time resolution of 1 min and the other measurements have a time resolution of 10 min.

example in Fig. 9 shows that we can observe anisotropies at high energies for electrons with HET. This example is one of three time periods found to show enhanced flux where we see anisotropies above the value of 1.

5. Summary and discussion

We report the first observations of electron anisotropies above 1 MeV with Solar Orbiter and show how Solar Orbiter's

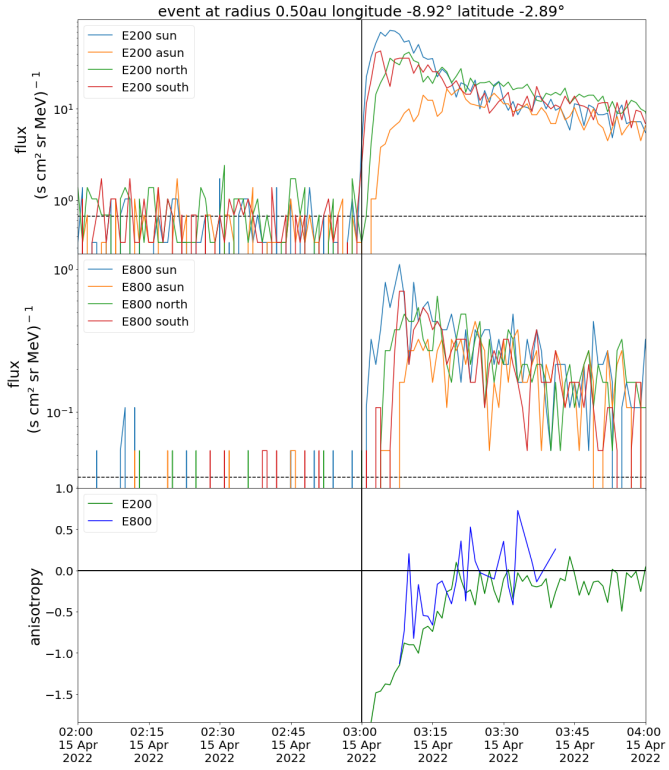

Fig. 9. Fluxes of the E200 (first panel) and E800 (second panel) electron channels of all four viewing directions of HET. In addition the anisotropy of the E200 (E800) channels is shown in blue (green) in the bottom panel.

EPD/HET can clearly perform this difficult measurement. Out of a list of 21 high-energy (>200 keV) electron time periods of enhanced flux, we find 3 with clearly anisotropic electron PADs above 1 MeV. All three anisotropic time periods were seen within 0.5 au, but several (5) other events seen within this distance from the Sun show no discernible anisotropy. The highest energies observable with HET (the E5700 channel) were seen in two events, neither of which showed a measurable anisotropy, both were observed well beyond 0.5 au; see Table 2.

Future observations of the PADs of relativistic electrons will provide limits on the transport properties of the inner heliosphere, which are an important factor for early warnings of approaching SEP events (Posner 2007). While the current list may include multiple relativistic electron events in one entry, discriminating between them by eye poses no difficulty. The focus here was to identify time periods of interest for studies of the properties of relativistic electron events. The automatic method used to identify these periods could certainly be improved; for example, by testing its sensitivity to variations of the detection threshold. The time period before the patch can be included in this procedure if further investigation of the data is carried out.

Acknowledgements. E.P.D. and this work were supported by the German Space Agency (Deutsches Zentrum für Luft- und Raumfahrt, e.V., DLR) under grant number 50OT2002 to the Kiel University. N.D. is grateful for support by the Academy of Finland (SHOCKSEE, grant no. 346902). Javier Rodríguez-Pacheco acknowledges the financial support by the Spanish Ministerio de Ciencia, Innovación y Universidades FEDER/MCIU/AEI Projects ESP2017-88436-R and PID2019-104863RB-I00/AEI/10.13039/501100011033. This work received funding from the European Union's Horizon 2020 research and innovation program under grant agreement No. 101004159 (SERPENTINE).

References

Agueda, N., & Lario, D. 2016, ApJ, 829, 131
Amano, T., Katou, T., Kitamura, N., et al. 2020, Phys. Rev. Lett., 124, 065101
Brüdern, M., Dresing, N. B., Heber, R. W.-S., et al. 2018, Cent. Eur. Astrophys. Bull., 42, 1
Dresing, N., Gómez-Herrero, R., Heber, B., et al. 2018, A&A, 613, A21
Dresing, N., Kouloumvakos, A., Vainio, R., & Rouillard, A. 2022, ApJ, 925, 12105
Dröge, W. 2000, ApJ, 537, 1073
Fletcher, L., Dennis, B. R., Hudson, H. S., et al. 2011, Space Sci. Rev., 159, 19
Gopalswamy, N., Yashiro, S., Krucker, S., Stenborg, G., & Howard, R. 2004, J. Geophys. Res., 109, 12105
Guo, F., & Giacalone, J. 2015, ApJ, 802, 97
Horbury, T. S., O'Brien, H., Carrasco Blazquez, I., et al. 2020, A&A, 642, A9
Hucke, S. 1990, Ph.D. Thesis, University of Karlsruhe, Germany
Kahler, S. W., Aurass, H., Mann, G., & Klassen, A. 2007, ApJ, 656, 567
Klein, K.-L., Krucker, S., Trottet, G., & Hoang, S. 2005, A&A, 431, 1047
Kouloumvakos, A., Nindos, A., Valtonen, E., et al. 2015, A&A, 580, A80
Kühl, P., & Heber, B. 2019, Space Weather, 17, 84
Kühl, P., Heber, B., Gómez-Herrero, R., et al. 2020, J. Space Weather Space Clim., 10, 53
Mewaldt, R. A., Cohen, C. M. S., Labrador, A. W., et al. 2005, J. Geophys. Res. Space Phys., 110, A09S18
Mitchell, J. G., Nolfo, G. A. D., Hill, M. E., et al. 2021, ApJ, 919, 119
Müller, D., Marsden, R. G., St. Cyr, O. C., et al. 2013, Sol. Phys., 285, 25
Müller, D., St. Cyr, O. C., Zouganelis, I., et al. 2020, A&A, 642, A1
Owen, C. J., Bruno, R., Livi, S., et al. 2020, A&A, 642, A16
Posner, A. 2007, Space Weather, 5, 05001
Reames, D. 1999, Space Sci. Rev., 90, 413
Rodríguez-Pacheco, J., Wimmer-Schweingruber, R. F., Mason, G. M., Ho, G. C., & Sènchez-Prieto, S. 2020, A&A, 642, A7
Terasa, C., Labrenz, J., Kühl, P., et al. 2013, Int. Cosmic Ray Conf., 33, 3627
Wibberenz, G., Kecskemety, K., Kunow, H., et al. 1989, Sol. Phys., 124, 353
Wimmer-Schweingruber, R. F., Janitzek, N. P., Pacheco, D., et al. 2021, A&A, 656, A22